Magnetic evidence for Yellow River sediment in the late Holocene deposit of the Yangtze River Delta, China

Feng Wang[a], Weiguo Zhang[a,*], Xiaomei Nian[a], Andrew P. Roberts[b], Xiang Zhao[b], Yuan Shang[a], Can Ge[c], Yan Dong[d]

[a] State Key Laboratory of Estuarine and Coastal Research, East China Normal University, Shanghai 200241, China
[b] Research School of Earth Sciences, Australian National University, Canberra, ACT 2601, Australia
[c] Zhejiang Institute of Hydraulics and Estuary, Hangzhou 310020, China
[d] Institute of Geographic Engineering Technology, School of Geographical Science, Nantong University, Nantong 226007, China

ABSTRACT

Sediment source identification is critical for understanding delta evolution processes and for managing delta sustainability, particularly for deltas experiencing significant recent fluvial sediment discharge. Sediment sources for the Yangtze River Delta (YRD) are commonly assumed to be derived from the Yangtze River, despite the fact that the YRD is a tide-dominated delta that can receive marine-sourced sediments in addition to fluvial inputs. In particular, potential contributions from the neighbouring sediment-laden Yellow River, when it discharged into the Yellow Sea during 1128–1855 CE, remains unclear. Here we present provenance analysis of three cores from the northern YRD using size-specific magnetic characterizations. We find that magnetic properties of sediments younger than ~400 years have large differences among the studied cores. Comparison of magnetic properties to potential sources, including the major Yangtze River tributaries (i.e., Jinsha River, Jialing River, and Han River) and Old Yellow River (OYR), indicates that the northern core received enhanced Yellow River sediment loads over the last 400 years, while the southern core had a dominant Yangtze influence, which is most pronounced in size fractions less than 16 μm. This interpretation is supported by geochemical results. The documented spatial sediment source heterogeneity is caused by differences in tidal-fluvial interaction among delta distributary channels. Our results imply that the neighbouring OYR delta to the north exerts a remote influence on the YRD through longshore transport. This coastal connectivity between deltas should be assessed when forecasting future tide-dominated delta changes in the context of global change.

1. Introduction

River deltas are sensitive to sediment supply, which are impacted by climate change and human activities (Syvitski et al., 2009). Due to their high population densities, economic activities, and vulnerability to climate and sea-level change, delta evolution research has received worldwide attention (e.g., Goodbred and Kuehl, 1999; Allison et al., 2003; Korus and Fielding, 2015; Chamberlain et al., 2018; Wang et al., 2018). Modern, global river sediment discharge has declined, which has strongly impacted the growth of many deltas in the world (Syvitski et al., 2009; Giosan et al., 2014; Yang et al., 2014). There is great interest in understanding quantitative linkages between sediment supply and delta growth (Yang et al., 2003; Gao, 2007; Wang et al., 2018; Besset et al., 2019). However, most studies address only fluvial supply; marine sediment inputs have been seldom considered. It has been

suggested that landward marine sediment transport contributes to tide-dominated delta buildup (Goodbred and Saito, 2012; Hoitink et al., 2017). This could partially explain why some deltas do not show obvious evidence of delta destruction despite the recent decline in fluvial sediment input (Besset et al., 2019). Numerous studies have shown that estuaries can impact each other along a coastline, so that the remote influence of neighbouring estuaries cannot be neglected (e.g., Giddings and MacCready, 2017).

The Yangtze River is the third largest river in the world. The population and economic center of China is situated on its delta. Due to dramatic environmental changes and significant human activities in the catchment (e.g., dam construction and forestation), modern sediment supply has declined 70% since the 1950s, which has led to a decreasing delta progradation rate, with erosion occurring in places (Yang et al., 2014). Delta erosion and sustainability has drawn great attention (Yang
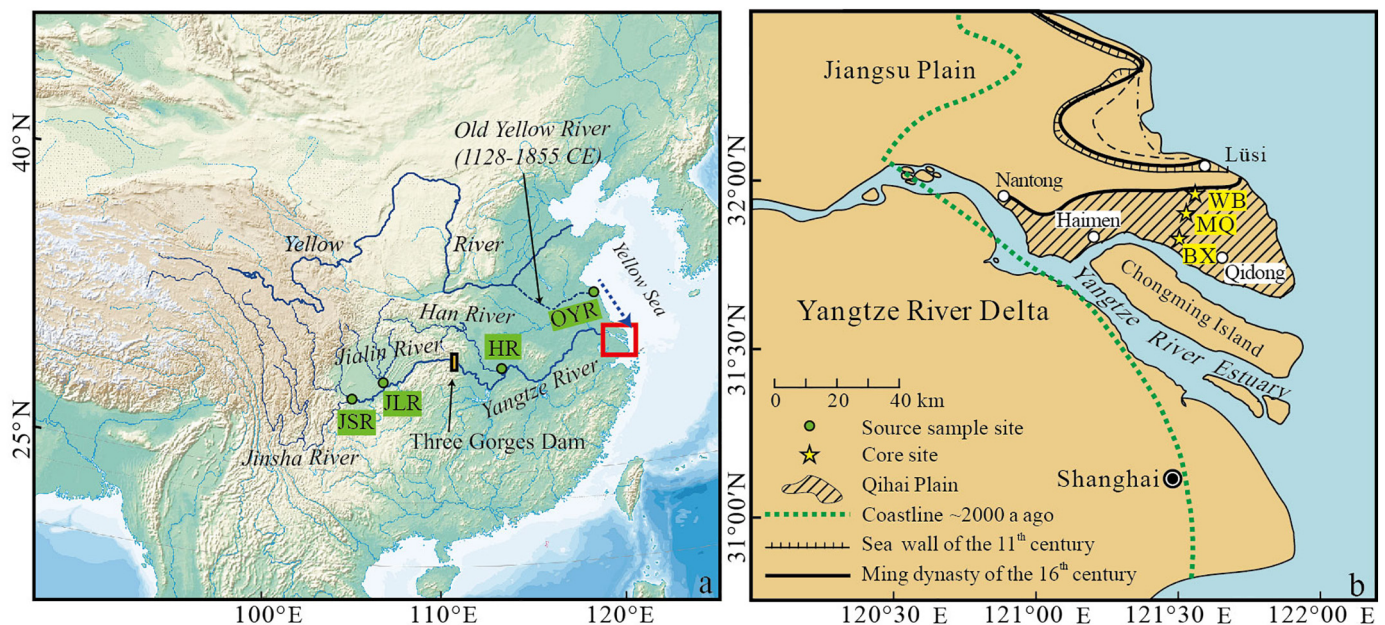

Fig. 1. (a) Location of the Yangtze and Yellow Rivers and the Yangtze River Delta (YRD) indicated with a red box that is shown in more detail in (b). Green boxes with abbreviated text represent major tributaries of the Yangtze River (JSR: Jinsha River, JLR: Jialing River, HR: Han River) and the Old Yellow River (OYR). (b) Schematic illustration of YRD coastline shifts over the last 2000 years (after Delta Research Group, 1978; Zhang, 1984), with core sites BX, MQ, and WB indicated as yellow stars. (For interpretation of the references to colour in this figure legend, the reader is referred to the web version of this article.)

et al., 2003; Gao, 2007; Wang et al., 2018). The Yangtze River Delta (YRD) is a tide-dominated delta, which means that there can be a potentially significant marine sediment supply to the delta. On the coast north of the YRD is the (abandoned) Old Yellow River (OYR) delta, which was formed by the Yellow River when it discharged into the Yellow Sea from 1128 to 1855 CE (Fig. 1). Historically, the Yellow River is one of the most turbid rivers in the world, with an annual sediment load of $1.0–1.6 \times 10^9$ t from 1370 to 1970 CE (Ren, 2015). Historical geography suggests that OYR sediment was transported southward by longshore currents and contributed to delta formation on the YRD in addition to the Yangtze River influence (e.g., Chu, 1987; Zhang, 2005). However, this hypothesis still lacks direct sedimentary evidence. To better understand YRD evolution and to contribute to forecasting of its future under changing climate and sea-level conditions, it is important to gain knowledge of sediment sources, particularly marine sources, from the neighbouring OYR delta.

Magnetic properties of sediments have been used to trace sediment sources in a variety of environments, in which the magnetic properties of sized fractions are used to minimize the influence of particle size (Hatfield and Maher, 2009; Liu et al., 2010b; Dong et al., 2014b; Hatfield et al., 2019). Our previous studies demonstrate that the Yangtze and Yellow River sediments can be distinguished magnetically (Zhang et al., 2008, 2012). Here we use an integrated environmental magnetic and geochemical approach on separated particle size fractions to understand YRD sediment sources over the last 1000 years, a period that covers the southern shift in course of the Yellow River. Our work has implications for understanding delta evolution and, hence, delta management in tide-dominated settings with possible influence of other coastal deltas.

2. Materials and methods

2.1. Study area and samples

The Yellow and Yangtze Rivers are two large rivers that deliver historically an annual average sediment load of ca 10×10^8 and 4.8×10^8 t to the sea, respectively, and play an important role in modifying China's central eastern coast (Milliman and Meade, 1983;

Yang et al., 2006). The modern YRD (Fig. 1b) formed from a paleo-incised valley over the last ca 8000 years as sea-level rose to its present-day level at a progressively decelerating rate (Chen et al., 1979; Song et al., 2013).

We collected three sediment cores (ca 23–26 m in length) from the northern part of the Yangtze River Delta, i.e., the Beixin (BX, 31°49′43″ N, 121°30′11″E), Miaoqiao (MQ, 31°54′14″ N, 121°30′59″E), and Wangbao (WB, 31°57′35.7″ N, 121°33′2.5″E) cores (Fig. 1). Each core contains prodelta facies, delta front facies, and delta plain facies in an ascending order. Our quartz optically stimulated luminescence (OSL) dating result indicates that the recovered sediments were deposited over the last 3,500 years, with the delta front and delta plain facies (the upper ca 18 m) starting to form in the last ~500 years (Fig. 2; Wang et al., 2019). Core MQ is located on a sandy river mouth bar, while cores BX and WB are from distributary channels within the delta (Wang et al., 2019). The studied cores were sectioned at 5 cm intervals. We selected samples at 15-cm stratigraphic intervals for this study, resulting in a total of 365 samples. The samples were dried at 40 °C for particle size, magnetic, and geochemical analyses.

Forty-eight core samples (16 from each core) were separated into five grain size fractions, i.e., < 16 μm, 16–32 μm, 32–63 μm, 63–125 μm, and > 125 μm. The > 63 μm fractions were separated by wet sieving, and were separated further based on Stokes' Law (Lu, 2000). Considering the dramatic influence of recent human activity (e.g., building of the Three Gorges Dam in 2003), the contribution of different tributaries to sediments discharged into the estuary has changed (Yang et al., 2014). Hence, we sampled at the terminus of the three major Yangtze River tributaries, i.e., the Jinsha, Jialing, and Han Rivers, which have markedly different sediment compositions (Yang et al., 2007; Chen, 2009; He et al., 2015) (Fig. 1a). In contrast, the Yellow River has sediment derived dominantly from the Chinese Loess Plateau, where sediments are homogeneous on a large spatiotemporal scale (Guo, 2010). We, therefore, sampled silts and clayey silts from the OYR delta to represent the Yellow River sediment endmember. Three surface samples were collected at each site, for a total of 12 samples (Fig. 1a).
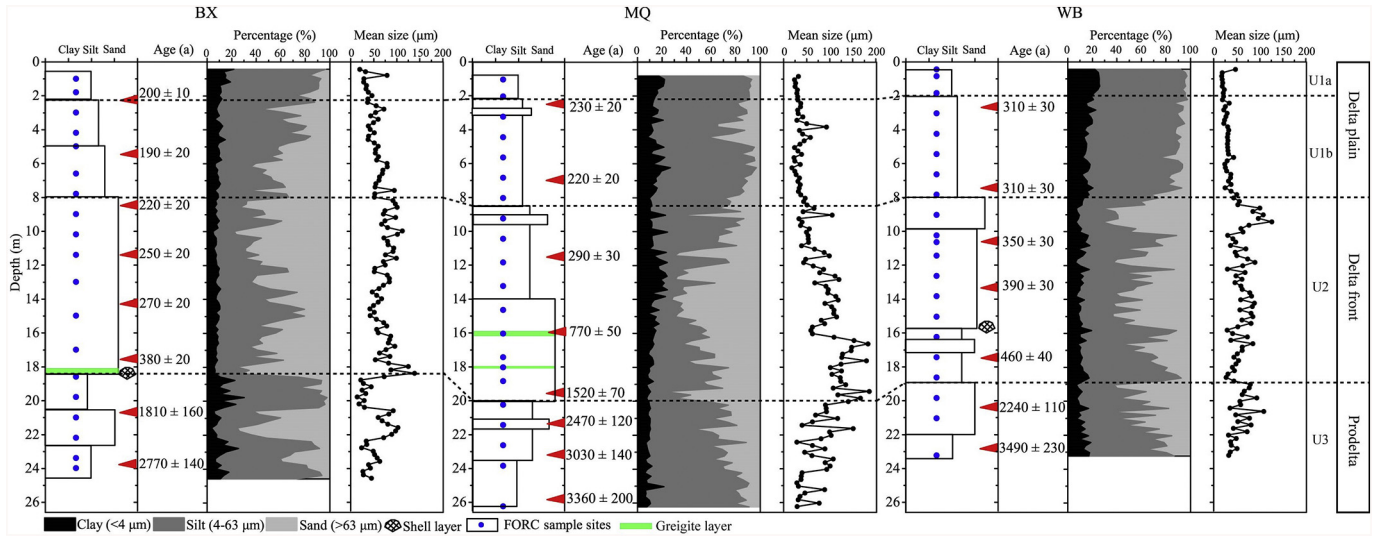
Fig. 2. Lithological log with down-core particle size variations and OSL ages for cores BX, MQ, and WB (after Wang et al., 2019). The triangles indicate depths for OSL datings data; solid circles indicate bulk samples used for first-order reversal curve (FORC) analysis.
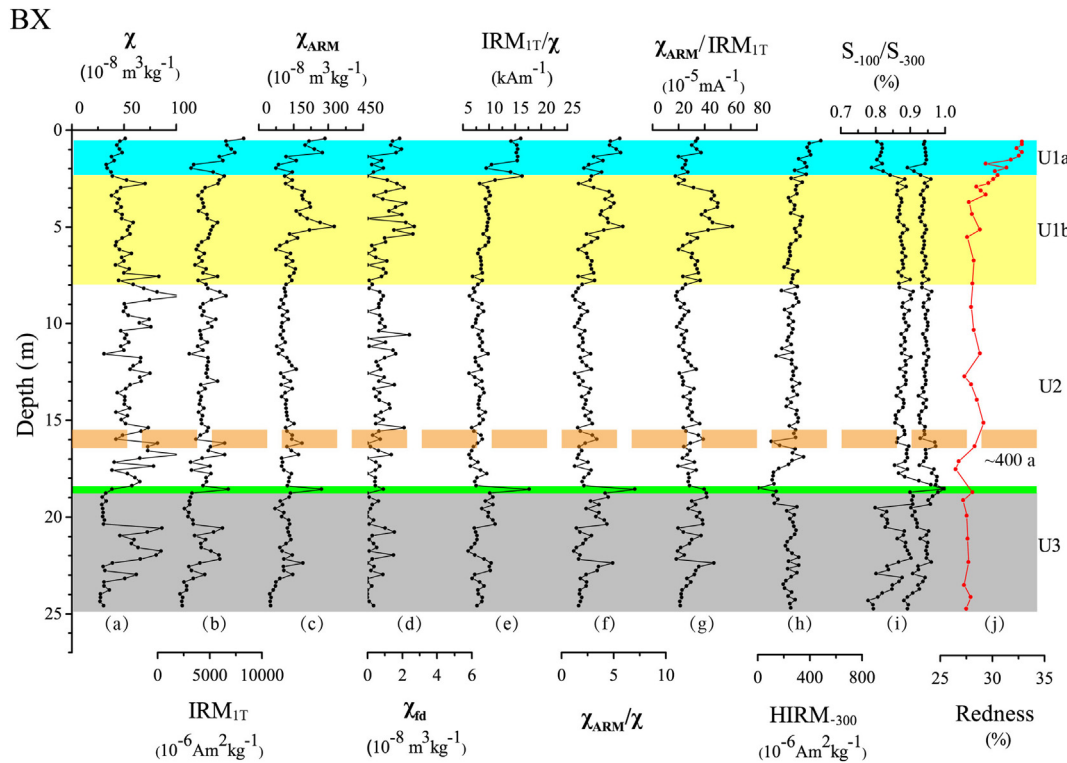

Fig. 3. Down-core (a-i) magnetic property and (j) redness variations (from DRS measurements) for core BX. The core is divided into units U3 (grey band) to U1 (blue band for U1a and yellow band for U1b) in ascending order. The green bar indicates a greigite-bearing layer; the dashed line represents depths corresponding to an age of *ca* 400 years before present as interpolated from OSL datings. (For interpretation of the references to colour in this figure legend, the reader is referred to the web version of this article.)

2.2. Methods

Low- (χ_{lf}, 0.47 kHz) and high- (χ_{hf}, 4.7 kHz) frequency magnetic susceptibility was measured using a Bartington Instruments MS2B magnetic susceptibility meter. Frequency-dependent susceptibility (χ_{fd}) was calculated as $\chi_{fd} = \chi_{lf} - \chi_{hf}$ in mass-specific terms. An anhysteretic remanent magnetization (ARM) was imparted with a peak alternating field (AF) of 100 mT and a direct current (dc) bias field of 0.04 mT using a DTECH 2000 AF demagnetizer. ARM is expressed as susceptibility of ARM (χ_{ARM}) by dividing the ARM by the dc field value used to

impart the ARM. An isothermal remanent magnetization (IRM) was imparted using an MMPM10 pulse magnetizer. Remanent magnetization measurements were made with an AGICO JR6 spinner magnetometer. IRMs imparted at 100 mT ($IRM_{-100\ mT}$) and 300 mT ($IRM_{-300\ mT}$) in the opposite direction to the IRM imparted at 1 T (IRM_{1T}) were measured to calculate the S-ratio (i.e., $S_{-x} = 100 \times (IRM_{1T} - IRM_{x\ mT})/(2 \times IRM_{1T})$) (Bloemendal and Liu, 2005). All IRM parameters are mass normalized. The 'hard' IRM ($HIRM_{-x}$) is defined as $HIRM_{-x} = (IRM_{1T} + IRM_{x\ mT})/2$, where x is either 100 mT or 300 mT.

Diffuse reflectance spectroscopy (DRS) measurements were made to
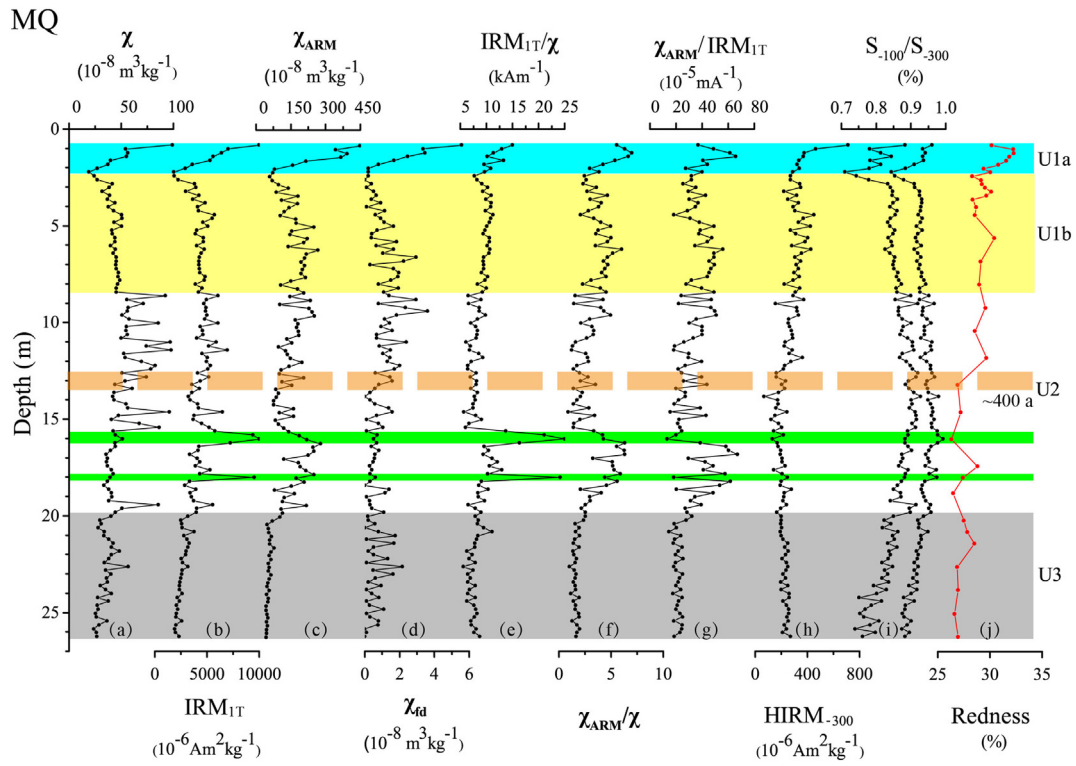
Fig. 4. Down-core (a-i) magnetic property and (j) redness variations for core MQ. The core is divided into units U3 to U1 in ascending order. Green bars indicate greigite-bearing layers; the dashed line represents the depth corresponding to an age of *ca* 400 years as interpolated from OSL datings. (For interpretation of the references to colour in this figure legend, the reader is referred to the web version of this article.)
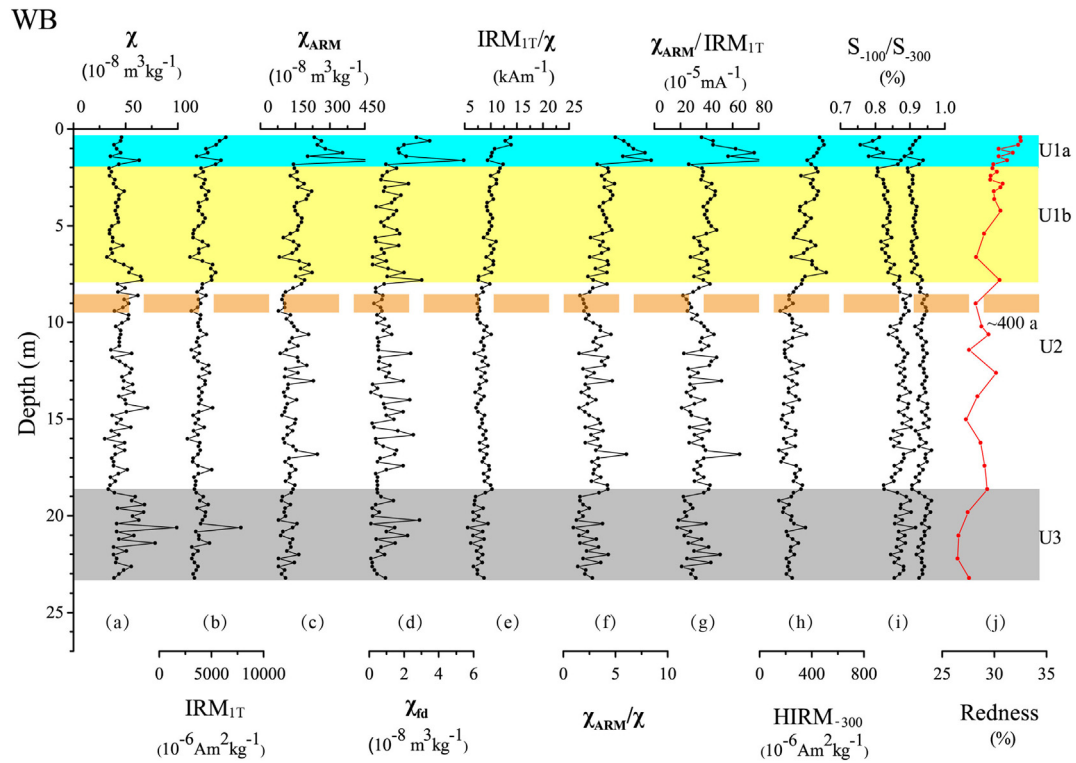

Fig. 5. Down-core (a-i) magnetic property and (j) redness variations for core WB. The core is divided into units U3 to U1 in ascending order. The dashed line represents the depth corresponding to an age of *ca* 400 years before present as interpolated from OSL dating. (For interpretation of the references to colour in this figure legend, the reader is referred to the web version of this article.)
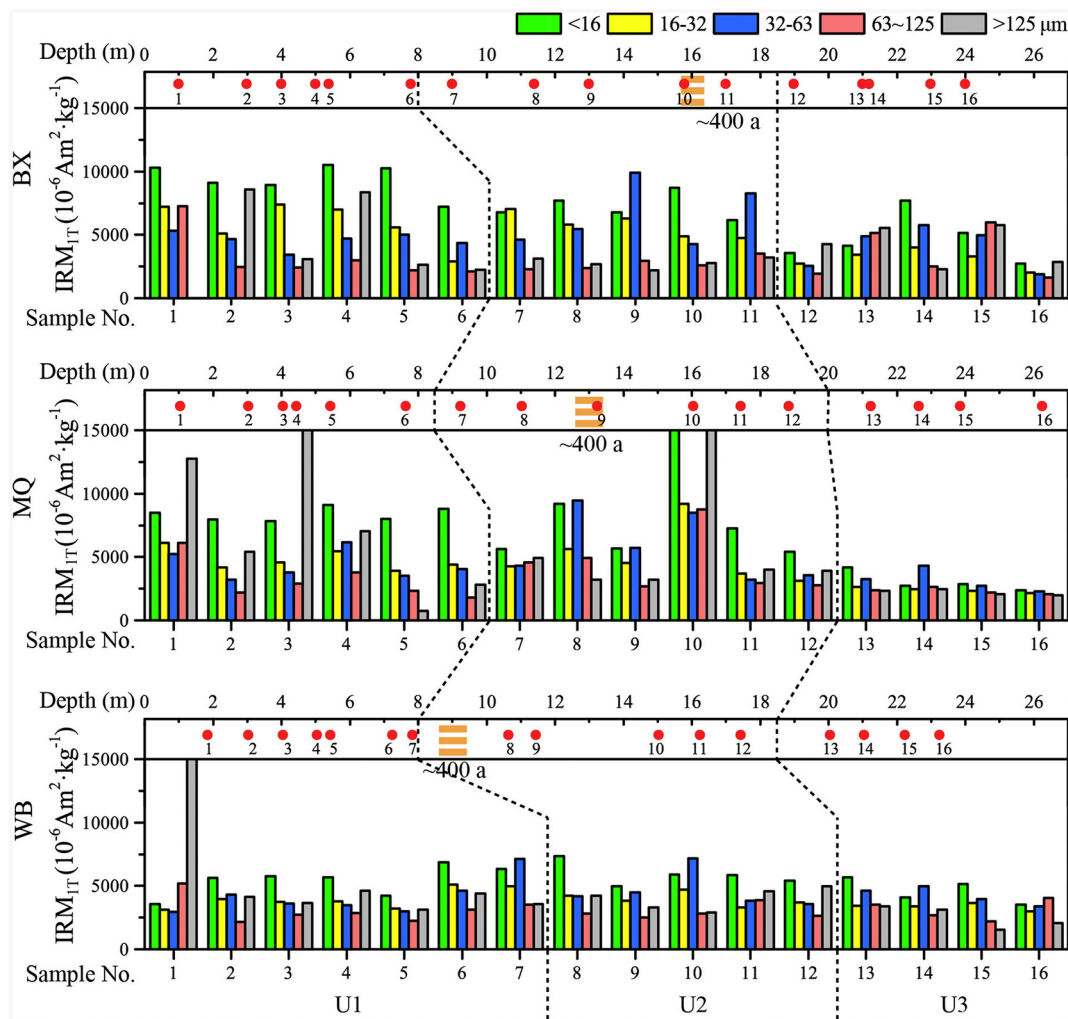
Fig. 6. Particle size specific IRM_{1T} variations for cores BX, MQ, and WB. Sample numbers and depths of corresponding samples are indicated on the lower and upper horizontal axes, respectively. The sample at 0.98 m in core BX has insufficient material in the > 63 μm fraction for magnetic measurements, so no data are available. The dotted lines mark the boundaries between units U1, U2, and U3, respectively. The thick dashed yellow line indicates an age of *ca* 400 years from OSL dating. (For interpretation of the references to colour in this figure legend, the reader is referred to the web version of this article.)

estimate hematite concentrations. DRS analyses were made as follows: samples from core depths above 3.5 m were measured at 20 cm intervals; measurements at lower depths were made at ~1 m intervals. DRS analyses were made over the 400–700 nm range at 1 nm intervals using a Perkin Elmer Lambda 950 spectrophotometer. The 630–700 nm red reflectance in standard colour bands is used to quantify hematite content (Torrent et al., 1980; Dong et al., 2014a). Magnetic and DRS analyses were made at the State Key Laboratory of Estuarine and Coastal Research, East China Normal University, Shanghai.

To characterize magnetic mineral assemblages, 140 first-order reversal curves (FORCs) were measured for each sample analyzed (Roberts et al., 2000) with a 1.57 mT field increment, a maximum applied field of 500 mT, and 200 ms averaging time. FORC measurements were made for 61 samples at ~1 m intervals throughout the studied cores. FORC diagrams were calculated using the FORCinel software v3.06 (Harrison and Feinberg, 2008). The FORC-principal component analysis (PCA) unmixing algorithm (part of the FORCinel package) of Harrison et al. (2018) was used to further characterize sedimentary magnetic particle assemblages to understand the magnetic particle fractions in the studied samples. VARIFORC parameters used to smooth PCA solutions are: $s_{c,0}$ = 5, $s_{c,1}$ = 8, $s_{b,0}$ = 5, $s_{b,1}$ = 8, and λ_c = λ_b = 0.1 (Egli, 2013). FORC measurements were made on representative samples (Fig. 2) with a Princeton Measurements Corporation MicroMag 3900 vibrating sample magnetometer (VSM) at the

Australian National University, Canberra.

χ and IRM_{1T} generally reflect the concentration of ferrimagnetic minerals, such as magnetite. χ has contributions from paramagnetic and diamagnetic minerals, while IRM_{1T} does not. IRM_{1T}/χ can be influenced by a number of factors, where, for example, a higher proportion of fine greigite can lead to higher values. χ_{fd} reflects the presence of fine viscous grains close to the superparamagnetic (SP)/single domain (SD) threshold size (Thompson and Oldfield, 1986). χ_{ARM} is sensitive to ferrimagnetic SD grains (Maher, 1988), and χ_{ARM}/χ and χ_{ARM}/IRM_{1T} are useful for detecting grain size changes (Banerjee et al., 1981; Liu et al., 2012). $HIRM_{-100}$ and $HIRM_{-300}$ are used commonly to estimate the concentration of medium- and high-coercivity minerals such as hematite and goethite. S_{-300} reflects relative variations of low-coercivity (e.g., magnetite and maghemite) to high-coercivity minerals, while S_{-100} reflects the relative abundance of low-coercivity minerals to medium- and high-coercivity minerals in the total assemblage (Liu et al., 2007; Yamazaki, 2009). PCA was carried out using the Origin-2018 software to identify statistically distinct magnetic property groups.

In order to assess magnetic interpretations, we measured Al, Fe, Ca, Na, K, Mg, Mn, Ti, Sr, Ba, V, Cr, and Ni concentrations on particle-sized fractions of samples younger than ~400 years and on source samples (total of 34 samples). The samples were digested with mixed $HF–HClO_4–HNO_3$ acid, and elements were determined with an
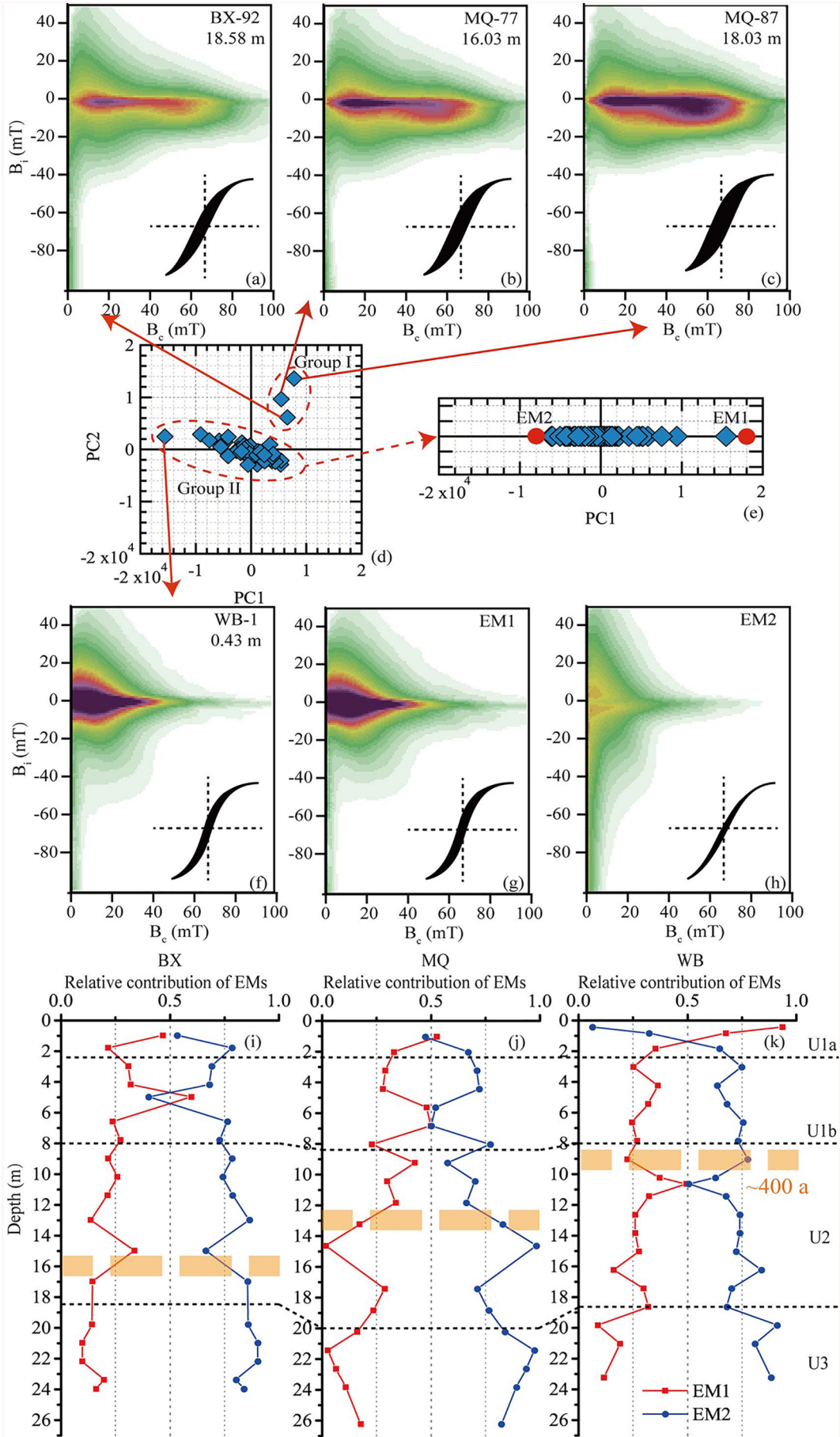
(caption on next page)

Fig. 7. FORC-PCA unmixing reveals two dominant data groups (Groups I and II (d)). Group I represents: (a-c) interacting stable SD greigite with vortex state iron oxides, while Group II represents (e) mixtures of two end members (EMs). EM1 represents (g) SD and vortex state magnetite and EM2 represents (h) vortex state and MD grains. Down-core relative contributions from EM1 and EM2 for cores (i) BX, (j) MQ, and (k) WB all indicate an increasing EM1 contribution from the base of the studied cores toward the surface.

inductively coupled plasma optical emission spectrometry (ICP-OES, Icap7000) (Zhang et al., 2009) at the East China Normal University, Shanghai. Quality control of analyses was checked with Chinese National Reference Material GSD9, which indicates an accuracy and precision better than 10%.

3. Results

3.1. Bulk magnetic properties

3.1.1. Core BX

Down-core magnetic property variations for core BX are shown in Fig. 3. χ and IRM_{1T} alternate between low and high values in unit U3 (24.6–18.8 m), with the lowest minima in the core. χ_{ARM} increases slightly up-core, while $HIRM_{-300}$ has relatively uniform values. In unit U2 (18.5–8.0 m), χ fluctuates significantly. By contrast, IRM_{1T}, χ_{ARM}, and $HIRM_{-300}$ have much smaller variations. χ declines upward in unit U1b (8.0–2.2 m) and then increases toward the surface in unit U1a (2.2–0.4 m). IRM_{1T} and $HIRM_{-300}$ are almost stable in unit U1b and then increase toward the surface in unit U1a. χ_{ARM} has a similar trend as IRM_{1T} and $HIRM_{-300}$ in unit U1a, but it also has a peak at 5.6–3.4 m in unit U1b (Fig. 3).

χ_{fd}, χ_{ARM}/χ, and χ_{ARM}/IRM_{1T} undergo similar changes throughout the core, with slight up-core increases and stable values to a depth of 5.6 m. Higher values occur at 5.6–3.4 m, which then decrease before increasing upward again in unit U1a. Apart from higher values in unit U1a and at 18.6 m, IRM_{1T}/χ undergoes no remarkable changes in other parts of the core. The S-ratio increases upward in unit U3, it remains stable in units U2 and U1b, and decreases upward in unit U1a. Notably, the sample at the boundary between units U3 and U2 (BX-92, 18.6 m) has high IRM_{1T}, χ_{ARM}, χ_{ARM}/χ, IRM_{1T}/χ, and S-ratio values, which are suggestive of the presence of greigite.

3.1.2. Core MQ

Down-core magnetic property variations for core MQ are shown in Fig. 4. In core MQ, χ, IRM_{1T}, χ_{ARM}, and χ_{fd} all have a generally increasing trend from unit U3 (26.2–20.0 m) to U2 (19.8–8.6 m). Starting at unit U1b (8.6–2.3 m), they then decrease up-core, while in unit U1a (above 2.3 m) they increase significantly to the surface. $HIRM_{-300}$ remains stable and low below ~13 m, and then increases gradually through U2 and U1b, and increases sharply in the uppermost sediments. χ_{ARM}/χ, χ_{ARM}/IRM_{1T}, and IRM_{1T}/χ have similar trends with depth. They are stable in U3, and increase upward before peaking at ~16 m. After decreasing from the peak at ~16 m, these parameters increase up-core to ~5 m, and then decrease toward the top of unit U1b. In unit U1a, IRM_{1T}/χ increases up-core to the surface, while χ_{ARM}/χ and χ_{ARM}/IRM_{1T} peak at 1.5 m. S-ratio increases up-core from the bottom of the core to peak at ~16.0 m, then declines toward the top of unit U1b, and then increases toward the surface in unit U1a. Two layers with high IRM_{1T}/χ values (16.0 m and 18.0 m) reflect the presence of greigite.

3.1.3. Core WB

Down-core magnetic property variations for core WB are shown in Fig. 5. χ, IRM_{1T}, and χ_{ARM} have variable but relatively stable values from unit U3 (23.2–19.0 m) to U1b (8.0–2.0 m). IRM_{1T} and χ_{ARM} have higher values in unit U1a (2.0 m to surface). $HIRM_{-300}$ is relatively stable from unit U3 to U2 (19.0–8.0 m), and then increases up-core in unit U1. χ_{ARM}/χ, χ_{ARM}/IRM_{1T}, and IRM_{1T}/χ have similar trends with depth. They are relatively stable in units U3 and U2 and increase up-core in unit U1b. In unit U1a, IRM_{1T}/χ increases to the surface, while

χ_{ARM}/χ and χ_{ARM}/IRM_{1T} have opposite trends. The S-ratio undergoes no remarkable changes in units U3 and U2 and decreases up-core in unit U1 except for increasing S_{-300} values in the upper 2 m of the core.

3.2. Magnetic properties of particle size fractions

Particle size specific values of IRM_{1T}, $HIRM_{-300}$, and S_{-100} are shown in Fig. 6 and S1–2. In unit U3 of all cores, IRM_{1T} is low and varies little with particle size. In units U2 and U1 of cores BX and MQ, IRM_{1T} generally increases with decreasing particle size, and peaks in the < 16 μm size fraction (Fig. 6). However, this feature is not evident in unit U1 of core WB, which has lower IRM_{1T} values and minor changes among particle size fractions. In general, $HIRM_{-300}$ is higher in the fine particle fraction (Fig. S1), while S_{-100} has the opposite trend (Fig. S2). The higher $HIRM_{-300}$ in the finer size fraction is consistent with the presence of hematite, which occurs in close association with clay minerals and will have lower S_{-100} values.

3.3. FORC unmixing

FORC unmixing results for typical samples are shown in Fig. 7. The samples are classified into two groups (Fig. 7d), where Group I is typical of greigite mixed with vortex state iron oxides (Fig. 7 a-c), which corresponds to samples with higher bulk IRM_{1T}/χ and S_{-300} values, and data for Group II fall along a linear trend, which is likely a mixture of two end members (EMs). EM1 consists of a mixture of fine SD and vortex state particles (Fig. 7g), while EM2 is a coarse detrital component dominated by vortex state and multidomain (MD) particles (Fig. 7h), by comparison with the expected FORC behavior of vortex state (Roberts et al., 2017; Lascu et al., 2018) and MD particles (Pike et al., 2001). The relative contributions of EMs in each core are shown in Fig. 7i-k. EM2 is dominant in the lower parts (unit U3) of the cores, with contributions > 75%. From unit U2 to U1b, the EM2 and EM1 contributions become more similar, and in uppermost unit U1a the EM1 contribution is > 50%. In unit U1a, the EM1 contribution in core WB is much higher than in cores BX and MQ, which have finer magnetic particle sizes than core WB.

3.4. DRS results

DRS redness results are shown in Fig. 3j, Fig. 4j, and Fig. 5j. In general, redness is lowest in unit U3 in each core and increases obviously toward the surface in unit U1a.

3.5. Geochemical results

A summary of elemental concentrations for samples younger than ~400 years in cores BX, MQ, and WB are shown in Table 1. The elements can be classified into two groups. Group 1 includes Al, Fe, K, Ti, Mn, Mg, Ba, V, Cr, and Ni, which decrease with increasing particle size. Group 2 includes Ca, Na, and Sr, which increase with increasing particle size. In the < 16 μm size fraction, the contents of Group 1 elements vary in the studied core as follows BX > MQ > WB, while Group 2 elements have the opposite trend. In the 16–32 μm size fraction, Al, K, Ca, Ba, and Cr have the opposite trend to the < 16 μm size fraction, while other elements have minor differences in the three cores. In the > 32 μm fractions, the elemental content difference among the cores are generally reversed for both Groups 1 and 2.

Table 1
Geochemical compositions (mean ± standard deviation) of samples younger than ~400 years in cores BX, MQ, and WB.

Size fraction	Core	Al (%)	Fe (%)	K (%)	Ca (%)	Na (%)	Mg (%)	Ti (%)	Mn (mg/kg)	Sr (mg/kg)	Ba (mg/kg)	V (mg/kg)	Cr (mg/kg)	Ni (mg/kg)
< 16 μm	BX (n = 10)	8.83 ± 0.41	6.14 ± 0.64	2.77 ± 0.21	1.90 ± 0.43	0.75 ± 0.10	1.97 ± 0.17	0.57 ± 0.05	1185 ± 213	120 ± 13	620 ± 47	148 ± 9	134 ± 24	65 ± 13
	MQ (n = 8)	8.32 ± 0.13	5.11 ± 0.37	2.75 ± 0.09	2.30 ± 0.22	0.81 ± 0.07	1.73 ± 0.12	0.59 ± 0.03	1043 ± 177	122 ± 6	554 ± 36	133 ± 7	114 ± 10	47 ± 4
	WB (n = 6)	8.34 ± 0.56	4.52 ± 0.36	2.58 ± 0.18	2.38 ± 0.36	0.85 ± 0.15	1.61 ± 0.05	0.56 ± 0.05	919 ± 66	124 ± 14	536 ± 38	118 ± 10	100 ± 10	41 ± 4
16–32 μm	BX (n = 10)	5.31 ± 0.49	2.79 ± 0.63	1.58 ± 0.14	3.16 ± 0.32	1.32 ± 0.12	1.35 ± 0.15	0.44 ± 0.04	524 ± 105	166 ± 18	401 ± 28	75 ± 14	55 ± 6	26 ± 8
	MQ (n = 8)	5.48 ± 0.29	2.52 ± 0.21	1.68 ± 0.09	2.90 ± 0.21	1.36 ± 0.06	1.26 ± 0.07	0.40 ± 0.03	515 ± 27	168 ± 8	424 ± 15	70 ± 6	58 ± 6	23 ± 2
	WB (n = 6)	5.87 ± 0.30	2.79 ± 0.34	1.78 ± 0.06	2.74 ± 0.09	1.24 ± 0.11	1.28 ± 0.05	0.42 ± 0.03	626 ± 100	160 ± 6	449 ± 27	77 ± 9	65 ± 7	26 ± 3
32–63 μm	BX (n = 10)	4.39 ± 0.18	2.09 ± 0.26	1.31 ± 0.10	3.30 ± 0.25	1.36 ± 0.05	1.14 ± 0.07	0.48 ± 0.09	418 ± 50	181 ± 12	344 ± 26	63 ± 10	48 ± 8	14 ± 3
	MQ (n = 8)	4.73 ± 0.25	2.19 ± 0.19	1.44 ± 0.12	3.05 ± 0.36	1.35 ± 0.05	1.14 ± 0.07	0.44 ± 0.10	450 ± 46	183 ± 15	377 ± 24	62 ± 8	54 ± 10	18 ± 1
	WB (n = 6)	5.15 ± 0.21	2.41 ± 0.28	1.54 ± 0.05	2.82 ± 0.07	1.26 ± 0.06	1.16 ± 0.05	0.42 ± 0.06	536 ± 85	172 ± 6	404 ± 14	66 ± 8	57 ± 8	21 ± 2
63–125 μm	BX (n = 10)	4.58 ± 0.38	1.86 ± 0.45	1.59 ± 0.17	2.84 ± 0.24	1.38 ± 0.06	0.99 ± 0.12	0.24 ± 0.03	326 ± 70	175 ± 7	427 ± 51	45 ± 10	32 ± 6	16 ± 5
	MQ (n = 8)	5.17 ± 0.64	2.68 ± 0.77	1.77 ± 0.29	2.77 ± 0.48	1.27 ± 0.07	1.17 ± 0.13	0.32 ± 0.07	570 ± 208	176 ± 14	470 ± 73	59 ± 10	61 ± 16	24 ± 8
	WB (n = 6)	5.58 ± 0.69	3.49 ± 1.13	1.86 ± 0.25	2.78 ± 0.33	1.15 ± 0.15	1.32 ± 0.19	0.33 ± 0.04	967 ± 432	170 ± 14	498 ± 55	69 ± 16	78 ± 25	33 ± 11
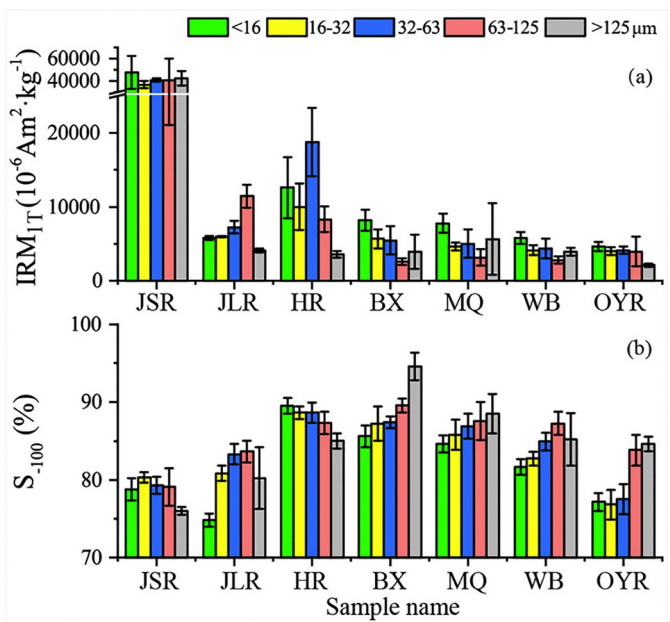
Fig. 8. Particle size specific (a) IRM_{1T} and (b) S_{-100} values for cores BX, MQ, and WB over the last 400 years and their comparison with four potential endmembers, i.e., JSR: Jinsha River; JLR: Jialing River; HR: Han River; and OYR: Old Yellow River. (For interpretation of the references to colour in this figure legend, the reader is referred to the web version of this article.)

4. Discussion

4.1. Influence of sediment particle size

Our particle size specific analysis demonstrates clearly that particle size has a strong influence on magnetic properties. In general, minor magnetic property variations occur across different particle size fractions in sediments in the lowest unit U3 of all cores, while differences are evident in sediments from the upper units U2 and U1. From *ca* 400 years to present-day, S_{-100} of the > 63 μm size fraction in core BX is much higher than in cores MQ and WB, while $HIRM_{-300}$ has the opposite relationship (Fig. S1–2). The proportion and concentration of high coercivity minerals in the coarsest particle sizes varies as WB > MQ > BX over the last 400 years. In units U2 and U1, the < 16 μm fraction generally has the highest IRM_{1T} and $HIRM_{-300}$ values, which suggests that both the low and high coercivity minerals are enriched in the finer particle size fractions (Fig. 6 and S1). The silt fraction (16–63 μm) contains fewer ferrimagnetic minerals. However, significantly higher IRM_{1T} values are not evident in the < 16 μm fractions at depths of *ca* 2 to 9 m in core WB, which is ascribed to a provenance difference as discussed below. Furthermore, minor magnetic property differences with particle size in unit U3 are explained by diagenesis, as discussed next.

4.2. Influence of diagenesis and pedogenesis

In each core, unit U3 has lower χ and IRM_{1T} both in bulk samples and particle size fractions. Furthermore, there are no obvious IRM_{1T} peaks in the finest < 16 μm fraction. This can be explained by diagenetic dissolution, which removes the finest magnetic grains first (Roberts, 2015). FORC unmixing has been used to assess diagenetic processes in reducing sedimentary environments, including dissolution in sulphidic environments (Roberts et al., 2018). Our FORC-PCA results are consistent with these findings and indicate that EM2 (coarse, detrital magnetic assemblage) dominates unit U3, which is consistent with overall initial magnetic coarsening in reducing environments. Ongoing iron oxide reduction will also cause hematite dissolution (Roberts,
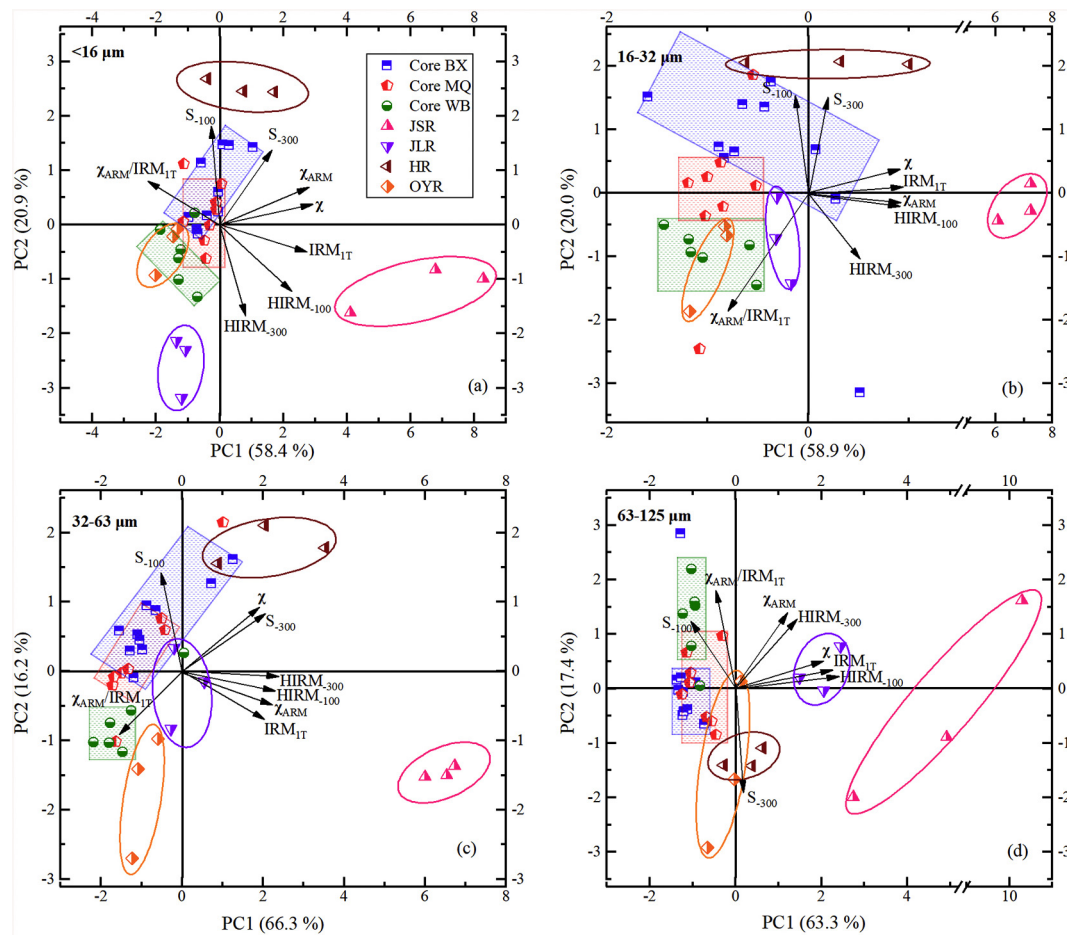
Fig. 9. Scatter plots of particle-sized fractions and magnetic properties on the first principal component (PC1) versus the second principal component (PC2). Results are shown for each size fraction: (a) < 16 μm, (b) 16–32 μm, (c) 32–63 μm, and (d) 63–125 μm. The ellipses mark PC score regions for data from the major tributaries of the Yangtze River (JSR: Jinsha River; JLR: Jialing River; HR: Han River) and the Old Yellow River (OYR). Rectangles are for core BX (blue), MQ (red), and WB (green), respectively. (For interpretation of the references to colour in this figure legend, the reader is referred to the web version of this article.)

2015), which explains low redness values in unit U3.

Increasing up-core redness also suggests that hematite contents increase toward the surface. This increase can be explained by increasing fine particle concentrations toward the surface because fine hematite is associated with finer soil particle sizes, although it is also likely that the local sedimentary environment became gradually more oxic as it was elevated above sea level (Dong et al., 2014a). The up-core S-ratio decrease in unit U3, especially in unit U1a, also indicates increased hematite proportions. The significantly increased EM1 (fine SD and vortex state) contribution in unit U1a may be related to fine-grained magnetite formation. Studies in nearby areas suggest that pedogenesis in surface sediments can lead to enrichment of oxidized magnetite, hematite, and goethite (Dong et al., 2014a).

4.3. Evidence of Old Yellow River sediments

Particle size specific IRM_{1T} and S_{-100} values for cores BX, MQ, and WB over the last 400 years and their comparison with four potential EMs are shown in Fig. 8. Among the EMs, Jinsha River has extremely high IRM_{1T} values, which is due to basaltic catchment rocks (Chen, 2009). The other three EMs have IRM_{1T} values in the range of delta sediments, with ranks as follows: Han River > Jialing River > OYR. S_{-100} values follow the Han River > OYR > Jialing River pattern for < 16 μm fraction. Therefore, the Jinsha River seems not to be a major historic source for delta deposits.

In general, IRM_{1T} and S_{-100} values are lower in core WB than in other cores, and are more similar to those of OYR (Fig. 8). To constrain

the sediment source, eight magnetic parameters (χ, IRM_{1T}, χ_{ARM}, $HIRM_{100}$, $HIRM_{300}$, S_{-100}, S_{-300}, and χ_{ARM}/IRM_{1T}) for particle-sized fractions were chosen for principal component analysis (PCA). The > 125 μm size fraction is not considered due to its small fraction of the total sediment (average content < 7%). The two extracted principal components (PCs) account for ~80% of the total variance for all size fractions (Fig. 9). The first PC (PC1) correlates positively with concentration-related parameters, which reflects mainly ferrimagnetic mineral concentration. PC2 has a close link to S_{-100} and reflects magnetic mineralogy.

Four potential source EMs can be distinguished clearly (Fig. 9). The < 63 μm fraction for the WB sediments is more similar to OYR sediments, while core BX sediments are more similar to Han River sediments (Yangtze River tributary). Data for samples from Core MQ are distributed between those for cores BX and WB (Fig. 9a-c). However, Han River and OYR samples cannot be separated clearly for the 63–125 μm fraction (Fig. 9d). Sediments in these cores have similar ages (< 400 years) and particle size compositions (Fig. 2), and the extent of their diagenetic modification appears to be similar. We, therefore, interpret these differences to reflect a change in sediment source in the different cores. Previous studies indicate that the Yangtze and Yellow Rivers are primary sediment sources for the coast around the YRD (Liu et al., 2010b; Zhang et al., 2012). Magnetically, Yangtze River sediments have higher IRM_{1T} and S_{-100} values compared to Yellow River sediments (Zhang et al., 2008, 2012). Our studies of Yangtze River tributary and OYR sediments confirm this conclusion (Fig. 9). Based on this evidence, we suggest that core WB received a
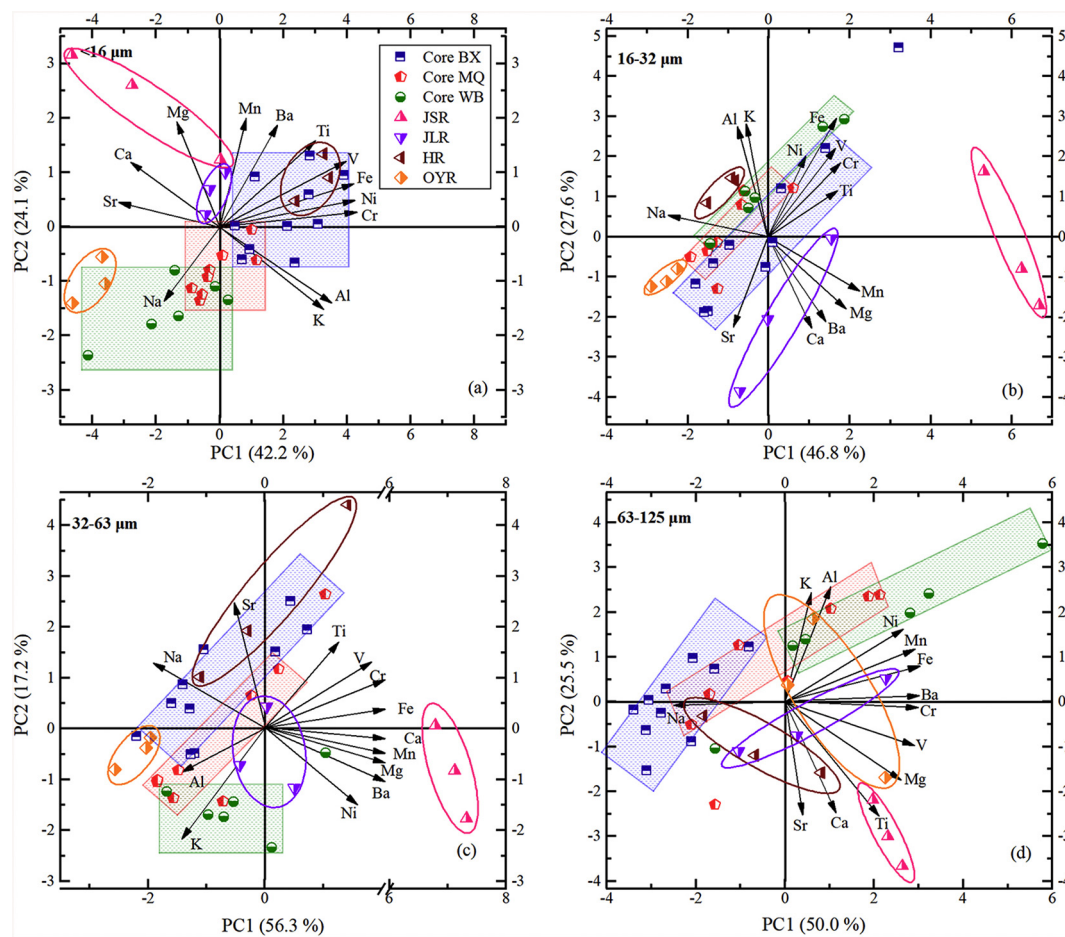
Fig. 10. Scatter plots of particle-sized fractions and geochemical compositions on the first principal component (PC1) versus the second principal component (PC2). Results are shown for each size fraction: (a) < 16 μm, (b) 16–32 μm, (c) 32–63 μm, and (d) 63–125 μm. The ellipses mark PC score regions for data from the major Yangtze River tributaries (JSR: Jinsha River; JLR: Jialing River; HR: Han River) and the Old Yellow River (OYR). The rectangles mark PC scores for data from core BX (blue), MQ (red), and WB (green), respectively. (For interpretation of the references to colour in this figure legend, the reader is referred to the web version of this article.)
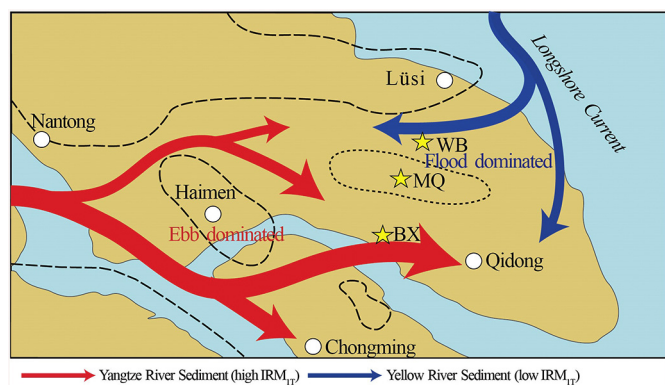
Fig. 11. Schematic diagram of landward and seaward sediment transport in the tide-dominated YRD and possible Yellow River contributions. The black line marks the modern coastline, while dashed and dotted lines represent the coastline and river mouth bar at the end of 16th century, respectively (after Tan, 1987). (For interpretation of the references to colour in this figure legend, the reader is referred to the web version of this article.)

greater sediment contribution from the OYR compared to the other two cores over the last 400 years.

PCA results for elemental composition variations are shown in Fig. 10. Previous studies have shown that Yangtze River sediments have higher Fe and Ti values, while Yellow River sediments have higher Ca,

Na, and Sr concentrations (Yang et al., 2002; Zhang et al., 2012; Zhou et al., 2015). In the < 16 μm size fraction, four potential source EMs can be distinguished clearly, with OYR sediments having higher Ca, Na, and Sr concentrations (Fig. 10a). Data for core WB are more similar to those for the OYR, while core BX data are more similar to those for Han and Jialing River (Yangtze River tributaries) sources. Core MQ data are distributed between those for cores BX and WB. This result is consistent with our environmental magnetic interpretations for the < 16 μm size fraction. For the coarser particle size fractions, ascription of core samples to a specific EM is not so direct (Fig. 10b-d), which might suggest that no single EM source controls the geochemical compositions of these fractions.

4.4. Remote influence of the Yellow River to the Yangtze River Delta

Based on historical documents, the Yellow River discharged into the Yellow Sea between 1128 and 1855 CE (Zhang, 1984; Ye, 1986). However, due to the presence of multiple Yellow River channels, the sediment load was evidently lower during the 1128–1578 CE interval. Starting from 1578 CE (ca 400 years ago), the river engineering strategy changed from "maintaining a broad flood plain with an embankment" to "clearing channel sediments by means of convergent flow" (Zhang, 1984; Ye, 1986). The former strategy caused a large amount of sediment to accumulate in the lower Yellow River reach, while the more recent strategy flushed greater amounts of sediment into the Yellow Sea, resulting in rapid progradation of the coast over the last 400 years

(Ye, 1986). Morphodynamic modelling has been used to simulate OYR delta growth (Su et al., 2017), which also reveals southward sediment transportation both before and after 1855, which is consistent with coastal progradation south to the OYR delta (Zhang et al., 1984). We infer that southward transportation of Yellow River sediment by the Yellow Sea Coastal Current was enhanced since 1578 CE, which promoted YRD aggradation and progradation (Wang et al., 2019). Analysis of a core from the subaqueous Yangtze River delta also reveals a strong OYR sediment signature over the last 600 years (Liu et al., 2010a).

Core MQ is located on a mouth bar, while cores WB and BX lie to the north and south of the mouth bar and are located in northern and southern distributary channels, respectively (Wang et al., 2019). Distributaries in a tide-dominated delta have different net sediment transportation directions due to tidal and river interaction (Hoitink et al., 2017). In flood-dominated distributaries, sediment is transported landward while in ebb-dominated distributaries, sediment is transported seaward (Chen, 1988; Nowacki et al., 2015). We suggest that core WB was located in a flood-dominated distributary, which imported and accumulated OYR derived sediment. Fine-grained sediment can be transported over long distances (Su et al., 2017), which can explain why core WB has markedly different magnetic properties in the < 16 μm fraction. In contrast, core BX is located in an ebb-dominated distributary and, therefore, accumulated a greater amount of Yangtze River sediment (Fig. 11). Core MQ, which is located between the two other cores, appears to have had a more balanced influence from the two rivers.

4.5. Implications for delta evolution studies

Our results support speculation about a possible Yellow River contribution to building the YRD (Chu, 1987; Zhang, 2005). Thus, for a tide-dominated delta like the YRD, marine contributions, including longshore transportation of delta/estuarine sediment from neighbouring deltas, should not be neglected. This connectivity between deltas/estuaries is not only limited to our study area, but is widespread in other areas, such as the North Pacific coast (Giddings and MacCready, 2017). This is critical for predicting delta evolution with declining fluvial discharge. It also calls for caution in using accumulated sediment volume in deltas to reconstruct past fluvial discharges.

While the three studied cores lie close to each other, spatial sediment source variations among the cores mean that delta deposits are highly heterogeneous. The exact mechanisms that produced spatial sediment source variations require further morphodynamic studies. Nevertheless, paleoenvironmental studies of closely-spaced sediment cores from deltaic environments can provide an improved understanding of these heterogeneous deposits, which can provide insight into delta evolution processes in tide-dominated settings.

5. Conclusions

Magnetic properties of sediments in three cores collected from the northern YRD over the last 400 years indicate variable sediment provenance. We find that sediments in the northern core WB are magnetically different from those in southern core BX, with intermediate features observed in the middle core MQ. Sediments from the northern core WB are closer to those of OYR sediment, while those of southern core BX are more like Yangtze River sediments, which is especially obvious in the < 16 μm size fraction. Geochemical analysis supports this interpretation. During the last 400 years, an increased Yellow River sediment discharge is evident along the coast north of the YRD. Our results demonstrate the influence of longshore coastal sediment transportation from the neighbouring river delta. This suggests that sediments from marine environments cannot be neglected when considering the evolution of tide-dominated deltas in the context of declining fluvial sediment discharges. Large spatial sediment source heterogeneity in the YRD suggests that higher sampling resolution of sediment cores is required to understand complex sediment transport and depositional processes in delta deposits.

Declaration of Competing Interest

The authors declare that they have no known competing financial interests or personal relationships that could have appeared to influence the work reported in this paper.

Appendix A. Supplementary data

Supplementary data to this article can be found online at https://doi.org/10.1016/j.margeo.2020.106274.

References

Allison, M.A., Khan, S.R., Goodbred, S.L., Kuehl, S.A., 2003. Stratigraphic evolution of the late Holocene Ganges−Brahmaputra lower delta plain. Sediment. Geol. 155, 317–342. https://doi.org/10.1016/S0037-0738(02)00185-9.

Banerjee, S.K., King, J., Marvin, J., 1981. A rapid method for magnetic granulometry with applications to environmental studies. Geophys. Res. Lett. 8, 333–336. https://doi.org/10.1029/GL008i004p00333.

Besset, M., Anthony, E.J., Bouchette, F., 2019. Multi-decadal variations in delta shorelines and their relationship to river sediment supply: an assessment and review. Earth-Sci. Rev. 193, 199–219. https://doi.org/10.1016/j.earscirev.2019.04.018.

Bloemendal, J., Liu, X., 2005. Rock magnetism and geochemistry of two Plio-Pleistocene Chinese loess-palaeosol sequences—implications for quantitative palaeoprecipitation reconstruction. Palaeogeogr. Palaeoclimatol. Palaeoecol. 226, 149–166. https://doi.org/10.1016/j.palaeo.2005.05.008.

Chamberlain, E.L., Tornqvist, T.E., Shen, Z., Mauz, B., Wallinga, J., 2018. Anatomy of Mississippi Delta growth and its implications for coastal restoration. Sci. Adv. 4, 4740. https://doi.org/10.1126/sciadv.aar4740.

Chen, J.Y., 1988. Dynamic Process and Geomorphological Evolution of the Yangtze River Estuary. Shanghai Science and Technology Publishers, Shanghai (in Chinese).

Chen, J.Y., Yun, C.X., Xu, H.G., Dong, Y.F., 1979. The developmental model of the Chang Jiang River estuary during last 2000 years. Acta Oceanol. Sin. 1, 103–111 (in Chinese with English abstract).

Chen, X., 2009. Characteristics of Sediments From the Main Tributaries of the Yangtze River and Their Implication for the Provenance Identification of the Sediments of the Yangtze Estuary. M.Sc. thesis. East China Normal University, Shanghai.

Chu, S., 1987. The evolution of Chongming Island. Geogr. Res. 6, 9–16 (in Chinese with English abstract).

Delta Research Group, Department of Marine Geology, Tongji University, 1978. Holocene formation and development of the Yangtze Delta. Chin. Sci. Bull. 35, 310–313 (in Chinese).

Dong, C., Zhang, W., He, Q., Dong, Y., Yu, L., 2014b. Magnetic fingerprinting of hydrodynamic variations and channel erosion across the turbidity maximum zone of the Yangtze Estuary, China. Geomorphology 226, 300–311. https://doi.org/10.1016/j.geomorph.2014.08.008.

Dong, Y., Zhang, W., Dong, C., Ge, C., Yu, L., 2014a. Magnetic and diffuse reflectance spectroscopic characterization of iron oxides in the tidal flat sequence from the coastal plain of Jiangsu Province, China. Geophys. J. Int. 196, 175–188. https://doi.org/10.1093/gji/ggt399.

Egli, R., 2013. VARIFORC: an optimized protocol for calculating non-regular first-order reversal curve (FORC) diagrams. Glob. Planet. Chang. 110, 302–320. https://doi.org/10.1016/j.gloplacha.2013.08.003.

Gao, S., 2007. Modeling the growth limit of the Changjiang Delta. Geomorphology 85, 225–236. https://doi.org/10.1016/j.geomorph.2006.03.021.

Giddings, S.N., MacCready, P., 2017. Reverse estuarine circulation due to local and remote wind forcing, enhanced by the presence of along-coast estuaries. J. Geophys. Res. Oceans. 122, 10184–10205. https://doi.org/10.1002/2016JC012479.

Giosan, L., Syvitski, J., Constantinescu, S., Day, J., 2014. Climate change: protect the world's deltas. Nature 516, 31–33. https://doi.org/10.1038/516031a.

Goodbred, S.L., Saito, Y., 2012. Tide-dominated deltas. In: Davis Jr, R.A., Dalrymple, R.W. (Eds.), Principles of Tidal Sedimentology. Springer, Dordrecht, pp. 129–149.

Goodbred, S.L.J., Kuehl, S.A., 1999. Holocene and modern sediment budgets for the Ganges-Brahmaputra river system: evidence for highstand dispersal to flood-plain, shelf, and deep-sea depocenters. Geology 27, 559. https://doi.org/10.1130/0091-7613(1999)027<0559:HAMSBF>2.3.CO;2.

Guo, Z., 2010. Loess geochemistry and Cenozoic paleoenvironments. Geochem. News 143, 1–10.

Harrison, R.J., Feinberg, J.M., 2008. FORCinel: an improved algorithm for calculating first-order reversal curve distributions using locally weighted regression smoothing. Geochem. Geophys. Geosyst. 9, Q5016. https://doi.org/10.1029/2008GC001987.

Harrison, R.J., Muraszko, J., Heslop, D., Lascu, I., Muxworthy, A.R., Roberts, A.P., 2018. An improved algorithm for unmixing first-order reversal curve diagrams using principal component analysis. Geochem. Geophys. Geosyst. 19, 1595–1610. https://doi.org/10.1029/2018GC007511.

Hatfield, R.G., Maher, B.A., 2009. Fingerprinting upland sediment sources: particle size-specific magnetic linkages between soils, lake sediments and suspended sediments. Earth Surf. Proc. Land. 34, 1359–1373. https://doi.org/10.1002/esp.1824.

Hatfield, R.G., Wheeler, B.H., Reilly, B.T., Stoner, J.S., Housen, B.A., 2019. Particle size specific magnetic properties across the Norwegian-Greenland Seas: insights into the influence of sediment source and texture on bulk magnetic records. Geochem. Geophys. Geosyst. 20, 1004–1025. https://doi.org/10.1029/2018GC007894.

He, M., Zheng, H., Clift, P.D., Tada, R., Wu, W., Luo, C., 2015. Geochemistry of fine-grained sediments in the Yangtze River and the implications for provenance and chemical weathering in East Asia. Prog. Earth Planet. Sci. 2. https://doi.org/10.1186/s40645-015-0061-6.

Hoitink, A.J.F., Wang, Z.B., Vermeulen, B., Huismans, Y., Kästner, K., 2017. Tidal controls on river delta morphology. Nat. Geosci. 10, 637–645. https://doi.org/10.1038/ngeo3000.

Korus, J.T., Fielding, C.R., 2015. Asymmetry in Holocene river deltas: patterns, controls, and stratigraphic effects. Earth-Sci. Rev. 150, 219–242. https://doi.org/10.1016/j.earscirev.2015.07.013.

Lascu, I., Einsle, J.F., Ball, M.R., Harrison, R.J., 2018. The vortex state in geologic materials: a micromagnetic perspective. J. Geophys. Res. Solid Earth 123, 7285–7304.

Liu, J., Saito, Y., Kong, X., Wang, H., Xiang, L., Wen, C., Nakashima, R., 2010a. Sedimentary record of environmental evolution off the Yangtze River estuary, East China Sea, during the last ~13,000 years, with special reference to the influence of the Yellow River on the Yangtze River delta during the last 600 years. Quat. Sci. Rev. 29, 2424–2438. https://doi.org/10.1016/j.quascirev.2010.06.016.

Liu, Q., Roberts, A.P., Torrent, J., Horng, C.S., Larrasoaña, J.C., 2007. What do the HIRM and S-ratio really measure in environmental magnetism? Geochem. Geophys. Geosyst. 8, Q9011. https://doi.org/10.1029/2007GC001717.

Liu, Q., Roberts, A.P., Larrasoaña, J.C., Banerjee, S.K., Guyodo, Y., Tauxe, L., Oldfield, F., 2012. Environmental magnetism: principles and applications. Rev. Geophys. 50, 197–215. https://doi.org/10.1029/2012RG000393.

Liu, S., Zhang, W., He, Q., Li, D., Liu, H., Yu, L., 2010b. Magnetic properties of East China Sea shelf sediments off the Yangtze Estuary: influence of provenance and particle size. Geomorphology 119, 212–220. https://doi.org/10.1016/j.geomorph.2010.03.027.

Lu, R., 2000. Soil and Agricultural Chemistry Analysis Method. China Agriculture Science and Technology Press, Beijing (in Chinese).

Maher, B.A., 1988. Magnetic properties of some synthetic sub-micron magnetites. Geophys. J. Int. 94, 83–96. https://doi.org/10.1111/j.1365-246X.1988.tb03429.x.

Milliman, J.D., Meade, R.H., 1983. World-wide delivery of river sediment to the oceans. J. Geol. 91, 1–21.

Nowacki, D.J., Ogston, A.S., Nittrouer, C.A., Fricke, A.T., Van, P.D.T., 2015. Sediment dynamics in the lower Mekong River: transition from tidal river to estuary. J. Geophys. Res. Oceans 120, 6363–6383. https://doi.org/10.1002/2015JC010754.

Pike, C.R., Roberts, A.P., Dekkers, M.J., Verosub, K.L., 2001. An investigation of multi-domain hysteresis mechanisms using FORC diagrams. Phys. Earth Planet. Inter. 126, 11–25. https://doi.org/10.1016/S0031-9201(01)00241-2.

Ren, M., 2015. Sediment discharge of the Yellow River, China: past, present and future—a synthesis. Acta Oceanol. Sin. 34, 1–8. https://doi.org/10.1007/s13131-015-0619-6.

Roberts, A.P., 2015. Magnetic mineral diagenesis. Earth-Sci. Rev. 151, 1–47. https://doi.org/10.1016/j.earscirev.2015.09.010.

Roberts, A.P., Pike, C.R., Verosub, K.L., 2000. First-order reversal curve diagrams: a new tool for characterizing the magnetic properties of natural samples. J. Geophys. Res. Solid Earth 105, 28461–28475. https://doi.org/10.1029/2000JB900326.

Roberts, A.P., Almeida, T.P., Church, N.S., Harrison, R.J., Heslop, D., Li, Y., Li, J., Muxworthy, A.R., Williams, W., Zhao, X., 2017. Resolving the origin of pseudo-single domain magnetic behavior. J. Geophys. Res. Solid Earth 122, 9534–9558. https://doi.org/10.1002/2017JB014860.

Roberts, A.P., Zhao, X., Harrison, R.J., Heslop, D., Muxworthy, A.R., Rowan, C.J., Larrasoaña, J.C., Florindo, F., 2018. Signatures of reductive magnetic mineral diagenesis from unmixing of first-order reversal curves. J. Geophys. Res. Solid Earth 123, 4500–4522. https://doi.org/10.1029/2018JB015706.

Song, B., Li, Z., Saito, Y., Okuno, J., Li, Z., Lu, A., Hua, D., Li, J., Li, Y., Nakashima, R., 2013. Initiation of the Changjiang (Yangtze) delta and its response to the mid-Holocene sea level change. Palaeogeogr. Palaeoclimatol. Palaeoecol. 388, 81–97. https://doi.org/10.1016/j.palaeo.2013.07.026.

Su, M., Yao, P., Wang, Z.B., Zhang, C.K., Stive, M.J.F., 2017. Exploratory morphodynamic modeling of the evolution of the Jiangsu coast, China, since 1855: contributions of old Yellow River-derived sediment. Mar. Geol. 390, 306–320. https://doi.org/10.1016/j.margeo.2016.10.013.

Syvitski, J.P.M., Kettner, A.J., Overeem, I., Hutton, E.W.H., Hannon, M.T., Brakenridge, G.R., Day, J., Vörösmarty, C., Saito, Y., Giosan, L., 2009. Sinking deltas due to human activities. Nat. Geosci. 2, 681–686.

Tan, Q., 1987. Historical Atlas of China. China Atlas Press, Beijing (in Chinese).

Thompson, R., Oldfield, F., 1986. Environmental Magnetism. Allen and Unwin, Winchester. https://doi.org/10.1007/978-94-011-8036-8.

Torrent, J., Schwertmann, U., Schulze, D.G., 1980. Iron oxide mineralogy of some soils of two river terrace sequences in Spain. Geoderma 23, 191–208.

Wang, F., Zhang, W., Nian, X., Ge, C., Zhao, X., Cheng, Q., Chen, J., Hutchinson, S.M., 2019. Refining the late-Holocene coastline and delta development of the northern Yangtze River delta: combining historical archives and OSL dating. Holocene 29, 1439–1449. https://doi.org/10.1177/0959683619985452.

Wang, Z., Saito, Y., Zhan, Q., Nian, X., Pan, D., Wang, L., Chen, T., Xie, J., Li, X., Jiang, X., 2018. Three-dimensional evolution of the Yangtze River mouth, China during the Holocene: impacts of sea level, climate and human activity. Earth-Sci. Rev. 185, 938–955. https://doi.org/10.1016/j.earscirev.2018.08.012.

Yamazaki, T., 2009. Environmental magnetism of Pleistocene sediments in the North Pacific and Ontong-Java Plateau: temporal variations of detrital and biogenic components. Geochem. Geophys. Geosyst. 10, 1525–2027. https://doi.org/10.1029/2009GC002413.

Yang, S., Li, C., Jung, H., Lee, H., 2002. Discrimination of geochemical compositions between the Changjiang and the Huanghe sediments and its application for the identification of sediment source in the Jiangsu coastal plain, China. Mar. Geol. 186, 229–241. https://doi.org/10.1016/S0025-3227(02)00335-3.

Yang, S., Belkin, I.M., Belkina, A.I., Zhao, Q., Zhu, J., Ding, P., 2003. Delta response to decline in sediment supply from the Yangtze River: evidence of the recent four decades and expectations for the next half-century. Estuar. Coast. Shelf Sci. 57, 689–699. https://doi.org/10.1016/S0272-7714(02)00409-2.

Yang, S., Jiang, S., Ling, H., Xia, X., Sun, M., Wang, D., 2007. Sr-Nd isotopic compositions of the Changjiang sediments: implications for tracing sediment sources. Sci. China Ser. D 50, 1556–1565. https://doi.org/10.1007/s11430-007-0052-6.

Yang, S., Milliman, J.D., Xu, K., Deng, B., Zhang, X., Luo, X., 2014. Downstream sedimentary and geomorphic impacts of the Three Gorges Dam on the Yangtze River. Earth-Sci. Rev. 138, 469–486. https://doi.org/10.1016/j.earscirev.2014.07.006.

Yang, Z., Wang, H., Saito, Y., Milliman, J.D., Xu, K., Qiao, S., Shi, G., 2006. Dam impacts on the Changjiang (Yangtze) River sediment discharge to the sea: the past 55 years and after the Three Gorges Dam. Water Resour. Res. 42, W4407. https://doi.org/10.1029/2005WR003970.

Ye, Q., 1986. On the development of the abandoned Yellow River delta in northern Jiangsu Province. Acta Geograph. Sin. 2, 112–122 (in Chinese with English abstract).

Zhang, R., 1984. Land-forming history of the Huanghe River delta and coastal plain of northern Jiangsu. Acta Geograph. Sin. 39, 173–184 (in Chinese with English abstract).

Zhang, W., Xing, Y., Yu, L., Feng, H., Lu, M., 2008. Distinguishing sediments from the Yangtze and Yellow Rivers, China: a mineral magnetic approach. Holocene 18, 1139–1145. https://doi.org/10.1177/0959683608095582.

Zhang, W., Feng, H., Chang, J., Qu, J., Xie, H., Yu, L., 2009. Heavy metal contamination in surface sediments of Yangtze River intertidal zone: an assessment from different indexes. Environ. Pollut. 157, 1533–1543. https://doi.org/10.1016/j.envpol.2009.01.007.

Zhang, W., Ma, H., Ye, L., Dong, C., Yu, L., Feng, H., 2012. Magnetic and geochemical evidence of Yellow and Yangtze River influence on tidal flat deposits in northern Jiangsu Plain, China. Mar. Geol. 319-322, 47–56. https://doi.org/10.1016/j.margeo.2012.07.002.

Zhang, X., 2005. The historical formation of Chongming Island. J. Fudan Univ. Soc. Sci. 3, 57–66 (in Chinese with English abstract).

Zhou, X., Li, A., Jiang, F., Lu, J., 2015. Effects of grain size distribution on mineralogical and chemical compositions: a case study from size-fractional sediments of the Huanghe (Yellow River) and Changjiang (Yangtze River). Geol. J. 50, 414–433. https://doi.org/10.1002/gj.2546.